Plasma physics and control studies planned in JT-60SA for ITER and DEMO operations and risk mitigation

M Yoshida[1,*] , G Giruzzi[2] , N Aiba[1], J F Artaud[2], J Ayllon-Guerola[3] , L Balbinot[4],
O Beeke[5], E Belonohy[6], P Bettini[4,7], W Bin[8], A Bierwage[1], T Bolzonella[4], M Bonotto[4],
C Boulbe[9], J Buermans[10], M Chernyshova[11], S Coda[12], R Coelho[13], S Davis[14], C Day[15],
G De Tommasi[16,17], M Dibon[18], A Ejiri[19], G Falchetto[2], A Fassina[4], B Faugeras[9], L Figini[8],
M Fukumoto[1], S Futatani[20], K Galazka[11], J Garcia[2] , M Garcia-Muñoz[3], L Garzotti[6],
L Giacomelli[8], L Giudicotti[4], S Hall[6], N Hayashi[1], C Hoa[21], M Honda[22], K Hoshino[23],
M Iafrati[24], A Iantchenko[12], S Ide[1], S Iio[25], R Imazawa[1], S Inoue[1], A Isayama[1], E Joffrin[2],
K Kamiya[1], Y Ko[19], M Kobayashi[26], T Kobayashi[1], G Kocsis[27], A Kovacsik[28],
T Kurki-Suonio[29], B Lacroix[2], P Lang[18], Ph Lauber[18], A Louzguiti[2], E de la Luna[30],
G Marchiori[4], M Mattei[16,17], A Matsuyama[1], S Mazzi[31], A Mele[16,17], F Michel[21], Y Miyata[1],
J Morales[2], P Moreau[2], A Moro[8], T Nakano[1], M Nakata[32], E Narita[1], R Neu[18], S Nicollet[2],
M Nocente[33], S Nowak[8], F P Orsitto[16], V Ostuni[2], Y Ohtani[1], N Oyama[1], R Pasqualotto[4],
B Pégourié[2], E Perelli[8], L Pigatto[4], C Piccinni[18], A Pironti[16,17], P Platania[8], B Ploeckl[18],
D Ricci[8], P Roussel[21], G Rubino[34], R Sano[1], K Särkimäki[29], K Shinohara[1,19], S Soare[35],
C Sozzi[8] , S Sumida[1], T Suzuki[1], Y Suzuki[32], T Szabolics[27], T Szepesi[27], Y Takase[19],
M Takech[1], N Tamura[1,32], K Tanaka[32], H Tanaka[36], M Tardocchi[8], A Terakado[1], H Tojo[1],
T Tokuzawa[32], A Torre[2], N Tsujii[19], H Tsutsui[25], Y Ueda[36], H Urano[1] , M Valisa[4], M Vallar[12],
J Vega[30], F Villone[16,17], T Wakatsuki[1], T Wauters[10], M Wischmeier[18], S Yamoto[1] and L Zani[2]

[1] National Institutes for Quantum Science and Technology, Naka, Ibaraki 311-0193, Japan
[2] CEA, IRFM, Saint-Paul-lez-Durance, F-13108, France
[3] University of Seville, 41012 Seville, Spain
[4] Consorzio RFX, I-35127 Padova, Italy
[5] Rudolf Peierls Centre for Theoretical Physics, University of Oxford, Oxford, OX1 3PU, United Kingdom
[6] CCFE, Culham Science Centre, OX14 3DB Abingdon, United Kingdom
[7] Department of Industrial Engineering, University of Padova, 35131 Padova, Italy
[8] Istituto di Scienza e Tecnologia del Plasma CNR, 20125 Milano, Italy
[9] Université de Nice, Nice, France
[10] Laboratory for Plasma Physics, LPP-ERM/KMS, Brussels, Belgium
[11] Institute of Plasma Physics and Laser Microfusion, Hery 23, 01-497 Warsaw, Poland
[12] EPFL, Swiss Plasma Center, CH-1015 Lausanne, Switzerland
[13] Instituto de Plasmas e Fusão Nuclear, Instituto Superior Técnico, Universidade de Lisboa, 1049-001 Lisboa, Portugal
[14] Fusion for Energy, D-85748 Garching, Germany
[15] Institute for Technical Physics, Karlsruhe Institute of Technology, Karlsruhe, Germany
[16] Consorzio CREATE, Napoli, Italy
[17] Università degli Studi di Napoli Federico II, Napoli, Italy
[18] Max-Planck-Institut für Plasmaphysik, D-85748 Garching, Germany

* Author to whom any correspondence should be addressed.

[19] The University of Tokyo, Kashiwa 277-8561, Japan

[20] Universitat Politècnica de Catalunya, Barcelona, Spain

[21] CEA, IRIG, 38000 Grenoble, France

[22] Kyoto University, Graduate School of Engineering, Kyoto 615-8530, Japan

[23] Faculty of Science and Technology, Keio University, Yokohama, Kanagawa 223-8522, Japan

[24] EUROfusion /ENEA, Centro Ricerche Frascati, Frascati, 00044 Roma, Italy

[25] Tokyo Institute of Technology, Tokyo 152-8550, Japan

[26] Graduate School of Engineering, Nagoya University, Nagoya 464-8603, Japan

[27] Centre for Energy Research, Konkoly-Thege 29-33, H-1121 Budapest, Hungary

[28] Institute of Nuclear Techniques, Budapest University of Technology and Economics, Budapest, Hungary

[29] Department of Applied Physics, Aalto University, Aalto, Finland

[30] Laboratorio Nacional de Fusion, CIEMAT, 28040 Madrid, Spain

[31] Aix-Marseille University, CNRS, PIIM, UMR, 7345 Marseille, France

[32] Institute for Fusion Science, Toki 509-5292, Japan

[33] Dipartimento di Fisica, Università degli Studi di Milano-Bicocca, Milano, Italy

[34] Università della Tuscia, Viterbo, Italy

[35] Institute of Cryogenics and Isotopic Technologies—ICIT, 240050 Râmnicu Valcea, Romania

[36] Graduate School of Energy Science, Kyoto University, Kyoto 606-8502, Japan

E-mail: yoshida.maiko@qst.go.jp

CrossMark

Abstract

A large superconducting machine, JT-60SA has been constructed to provide major contributions to the ITER program and DEMO design. For the success of the ITER project and fusion reactor, understanding and development of plasma controllability in ITER and DEMO relevant higher beta regimes are essential. JT-60SA has focused the program on the plasma controllability for scenario development and risk mitigation in ITER as well as on investigating DEMO relevant regimes. This paper summarizes the high research priorities and strategy for the JT-60SA project. Recent works on simulation studies to prepare the plasma physics and control experiments are presented, such as plasma breakdown and equilibrium controls, hybrid and steady-state scenario development, and risk mitigation techniques. Contributions of JT-60SA to ITER and DEMO have been clarified through those studies.

Keywords: JT-60SA, plasma control, risk mitigation, scenario development

(Some figures may appear in color only in the online journal)

1. Introduction

The major objectives of the JT-60SA project are to achieve fully noninductive steady-state operations above the no-wall ideal magnetohydrodynamic (MHD) stability limits for a time much longer than the current diffusion time, as well as scenario development and risk mitigations for ITER. JT-60SA is a large fully superconducting tokamak device with high plasma current, I_p of 5.5 MA, high auxiliary power and long pulse ($P_{aux} = 41$ MW for 100 s), and highly shaped plasmas. The high shaping factor of $S = q_{95}I_P/(a_P B_T) \sim 7$, the aspect ratio of $A \sim 2.7$, the elongation of $\kappa_x \sim 1.9$, the triangularity of $\delta_x \sim 0.5$ are accessible as well as ITER and DEMO-like shapes. Here q_{95}, a_P, and B_T are the safety factor at 95% of magnetic flux surface, plasma minor radius, and the toroidal magnetic field respectively. These machine characteristics will enable us to address the key physics issues for plasma physics and control studies in ITER and DEMO-relevant regimes [1]. Here the DEMO represents a steady-state high normalized beta (β_N) reactor in this paper, for instance, Slim CS and JA DEMO2014 [2]. On the other hand, operation regimes will be explored as a broad spectrum of DEMO concepts around the reference designs.

The JT-60SA tokamak was fully assembled in March 2020 and the Integrated Commissioning started in September 2020 with vacuum pumping of the vacuum vessel and cryostat [3]. The toroidal and poloidal magnetic-filed coils reached a superconducting level with very careful temperature control in the coil systems to avoid the thermal stress. The full toroidal magnetic field coil current of 25.7 kA (corresponded to $B_T = 2.25$ T at the plasma center) was sustained with a stable coil temperature. Fast voltage control of ~ 500 kV s^{-1} on the

Table 1. Plan for research phases with key components.

Phase	NBI[2]		ECRF[3]	Divertor	First wall
	P-NB	N-NB			
Initial Research[1]	0	0	1.5 MW	CFC upper[4]	Graphite and Stainless
Initial Research II	6 MW	10 MW	3 MW	Intertial cooled CFC	CFC and Graphite
Initial Research III	13.5MW				
Integrated Research I	20 MW		7 MW	Active cooled CFC	
Integrated Research II				Monoblock type tungsten	Tungsten
Extended Research	24 MW			TBD	TBD

[1] Main gas in the Initial Research Phase I is H, that in the latter phases is D.

[2] Pulse length of P-NB and N-NB is 100 s, duty cycle is 1/30.

[3] ECRF frequencies are 82, 110 and 138 GHz. Pulse length of ECRF is depend on the frequency and research phase (see [1] for more details).

[4] Upper Divertor is used in the early of Initial Research Phase I, lower divertors will be equipped in the latter phases.

poloidal field coils were validated to be applied to plasma breakdown and plasma shape control. Next steps are to demonstrate plasma breakdown and optimization of equilibrium control up to $I_p \sim 2.5$ MA in a divertor configuration using the toroidal and poloidal superconducting coils. Electron cyclotron wall cleaning operations will be also explored by scanning the EC parameters, gas puff ratio, and horizontal magnetic fields.

Plasma control schemes and operation scenarios have been developed in many tokamaks by taking advantage of these machine characteristics. The EAST, KSTAR and WEST machines have developed long pulse operations with superconducting coils [4–6]. The JET, DIII-D, TCV machines have explored high beta and/or steady-state physics [7–9]. ITER risk mitigation studies, such as disruption control, edge localized mode (ELM) control, and divertor power and particle handling schemes have been conducted in many devices. The JT-60SA program will focus on scenario development and risk mitigation in ITER and DEMO relevant regimes. Modeling studies and subsystem feasibility studies have been carried out by the JT-60SA Research Units to simulate the operation scenarios and key elements on JT-60SA [10].

A logical sequence organized in different research phases is shown in table 1 [1]. Heating power and divertor will be enhanced according to the research phase. Initial Research Phase I with hydrogen plasmas will concentrate on commissioning of the plasma equilibrium controllability up to the full plasma current. From the Initial Research Phase II with deuterium plasmas, the physics and controllability of ITER and DEMO relevant high confinement and/or high beta plasmas will be assessed by using benefits of the carbon wall condition, to provide reliable theoretical models and control schemes for ITER and DEMO. Risk mitigation studies for ITER and DEMO will also be investigated with the high power and enhanced subsystems. In the Integrated Research Phase I, a compatibility of high density, high beta, high confinement and radiative divertor will be explored using the upgraded power and divertor performance. After the mission goal and major objectives are achieved, both the materials of the first wall and

divertor will change to tungsten. The metal wall experiments will begin in the Integrated Research Phase II to support the ITER full power phase.

The paper presents the main results of preparatory studies for the above-mentioned issues on JT-60SA and describes JT-60SA contributions for ITER on plasma physics and first ITER campaigns.

2. JT-60SA operation area

The main parameters of typical operation scenarios are shown in table 2. The operation scenario (I) with full plasma current of 5.5 MA, full auxiliary heating power of 41 MW, and high shape ($A = 2.51$, $\kappa_x = 1.87$, $\delta_x = 0.50$) is advantageous for transport, MHD and pedestal studies because of the large dynamic range of the collisionality, ν^* and gyroradius, ρ^* in ITER and DEMO regimes. The maximum heating power will be 41 MW with the negative-ion-based neutral beam (N-NB) of 10 MW, positive ion based neutral beam (P-NB) of 24 MW and electron cyclotron heating (ECH) of 7 MW. The ITER standard scenario (II) and hybrid scenario (III) will be developed at high plasma current around $I_P \approx 3.5$–4.6 MA, $B_T \approx 2.28$ T and $q_{95} \approx 3.2$–4.4 with an ITER-like shape configuration ($\delta_x \approx 0.41$, $\kappa_x \approx 1.81$). The hybrid scenario in JT-60SA is associated with the ITER hybrid plasma (scenario 3) with the main conditions of a weakly reversed shear ($q > 1$), $q_{95} \sim 4$, mild $\beta_N > 2$, the non-inductive fraction of about 0.5, and higher $H_{98(y,2)} > 1$ without critical neo-classical tearing modes. The steady-state high β_N scenario (IV) will be developed at medium plasma current of $I_P \approx 2.3$ MA, $B_T \approx 1.72$ T and $q_{95} \approx 5.8$ with a DEMO-like shape configuration ($A \approx 2.68$, $\delta_x \approx 0.47$, $\kappa_x \approx 1.90$, $S \approx 7.0$). The high-power long pulse of about 100 s is compatible with the actively cooled divertor and reduced heat flux onto the divertor of 10–15 MW m^{-2}.

Tackling the scenario development for ITER and DEMO is a high priority as well as the ITER risk mitigation in the Initial Research Phase II. Both NB and electron cyclotron range of frequency (ECRF) will be ready to be injected in long pulses (up to 100 s). On the other hand, the pulse duration with high

Table 2. Parameters of the main operation scenarios.

| Parameters	(I) Full I_P and full power	(II) ITER like inductive	(III) Hybrid	(IV) High β_N steady-state
Plasma current, I_P (MA)	5.50	4.60	3.50	2.30
Toroidal magnetic field, B_T (T)	2.25	2.28	2.28	1.72
Safety factor, q_{95}	3.0	3.2	4.4	5.8
Major radius, R_P (m)	2.96	2.93	2.93	2.97
Minor radius, a (m)	1.18	1.14	1.14	1.11
Aspect ratio, A	2.51	2.57	2.57	2.68
Elongation, κ_x	1.87	1.81	1.8	1.90
Triangularity, δ_x	0.50	0.41	0.41	0.47
Shape factor ($=q_{95}I_p/(aBt)$)	6.3	5.7	5.9	7.0
Heating power, P_{aux} (MW)	41	20	37	23
Flattop duration (s)	100	100	100	100
Volume averaged electron density (m^{-3})	5.6×10^{19}	8.1×10^{19}	6.2×10^{19}	4.2×10^{19}
Normalized density, n_e/n_{GW}	0.5	0.8	0.8	0.9
Confinement improvement, $H_{98(y,2)}$	1.3	1.0	1.2	1.6
Normalized beta, β_N	3.1	2.1	3.0	4.3
Bootstrap current fraction, f_{BS}	0.3	0.3	0.4	0.7
Plasma volume (m^3)	131	122	122	124
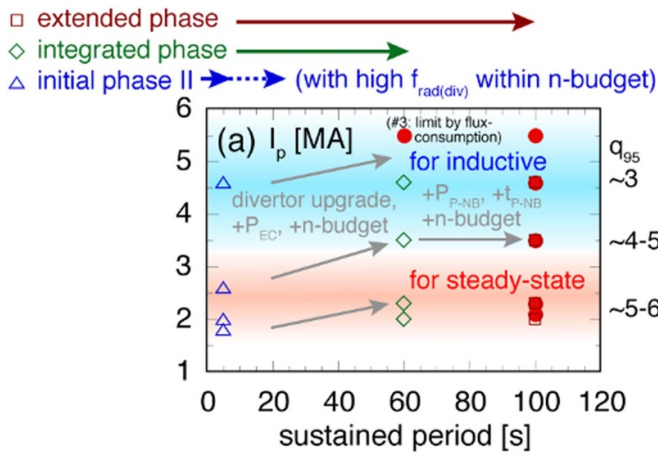
Figure 1. Progress of operation regime development in plasma current and sustained period. Gray arrows show machine capability upgrades. Red circles show the typical operation scenarios with full machine capability. Triangles, diamonds, and squares show the scenarios as examples of possible scenarios within the machine capability in Initial Research Phase II, Integrated Research Phase and Extended Research Phase, respectively.

Figure 2. (a) Non-dimensional plasma parameter regimes. Transport experiment can be performed at ITER-relevant normalized collisionality (ν^*), poloidal Larmor radius (ρ_p^*). JT-60U (cloud) and JET hybrid plasmas (inverted triangles) are also shown. (b) Volume averaged energetic ion beta, $<\beta_h>$, versus the energetic particles thermal velocity normalized to the Alfvén velocity, V_f/V_A.

power heating will be limited by the allowable heat flux onto the inertially cooled carbon fiber composite (CFC) divertor plate (15 MW m^{-2} × 5 s). The duration could shorter than the current diffusion time of the target ITER-like plasmas and steady-state plasmas in JT-60SA. Thus, the main objective of the Initial Research Phase II is to access the ITER standard-plasmas, and high β_N regimes above the no-wall ideal MHD stability limits. Current ramp-up scenarios will be developed by avoiding critical MHD modes and collapse in order to obtain a q profile with target plasma parameters (β_N $H_{98y,2}$, etc) of each scenario (figure 1). Then, the pulse duration and plasma parameters will be expanded in the Integrated Research Phase I where the inertial CFC divertors will be replaced by actively cooled divertors.
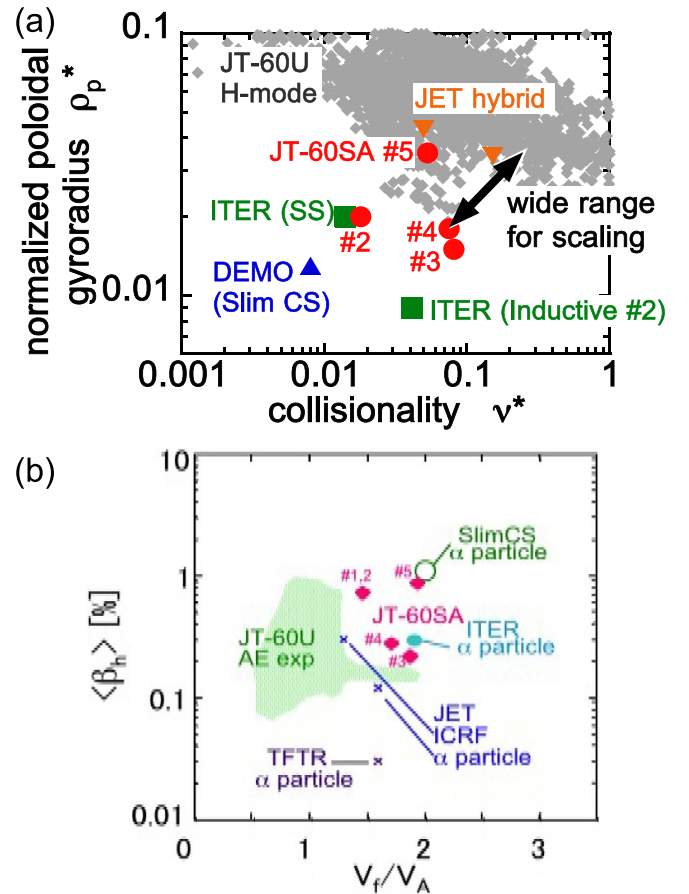
The high heating power and high plasma current will also enable us to study plasma physics and plasma controllability in

the ITER and DEMO regimes of important non-dimensional parameters: the normalized beta, the bootstrap current function, the normalized collisionality, the normalized Larmor radius, and electron heating ratio in ITER- and DEMO-like plasma shapes. Figure 2(a) shows an example of the normalized parameters in JT-60SA comparing those in ITER and DEMO. Core-edge transport and confinement studies can be performed at ITER-relevant normalized collisionality, poloidal Larmor radius, $\rho_p{}^*$ as well as in high β_N and dominant electron heating conditions. Although the energetic ions in JT-60SA are mainly beam ions produced by the N-NB, JT-60SA will provide important aspects of MeV-class energetic particles physics in the ITER and DEMO-relevant regimes, such as fast ion beta, β_h and the energetic particle thermal velocity, V_f/V_A as shown in figure 2(b). The physics basis of high energy particles will be investigated, for instance, energetic particle driven mode studies and energetic particle effects on transport and confinement, in to contribute to ITER and DEMO operations and modeling.

3. Plasma physics and control studies

3.1. Plasma start-up

The first target of the plasma control studies will be plasma breakdown and equilibrium control up to the full-plasma current using the superconducting central solenoid (CS) and equilibrium field (EF) coils (figure 3(a)). Advanced computational codes and control logics have been developed, such as premagnetic optimization scheme for the breakdown, plasma equilibrium control with isoflux scheme, control gain optimization methods, and strategies for accessing stable operational regimes.

A breakdown optimization method has been developed based on the inverse reconstruction of the magnetic fluxes using the external magnetic sensors [11]. The motivation of this code development is to minimize the number of required shots to optimize the magnetic flux distribution, even if the passive structure model is different from the real one. The coil voltage is calculated to minimize the gap between the target and measured magnetic fields. Then, the coil voltage is given as a modified command value. The inverse reconstruction method is applied to JT-60SA under the conditions of CS coil current of $I_{CS} = 6$ kA, toroidal magnetic field of 2.42 T at the center of the breakdown target, passive structures of vacuum vessel, and 27 magnetic flux loops and 17 magnetic probes. Figure 3(b) shows an example of a failure case due to the difference of the modeled passive structure with the real one. The field null area of <10 G is very narrow as shown in the hatched regions. Such a deviation can occur due to the complex passive structure of the vacuum vessel, port, cryostat, and so on. Figure 3(c) shows an optimized field null configuration (FNC) calculated by this method. The mean deviation of the stray field strength, ΔB_p in the breakdown target region decreases with the number of iterations, n as shown in figure 3(d). Here the requirement of the stray field is evaluated less than 10 G. This means that the breakdown magnetic
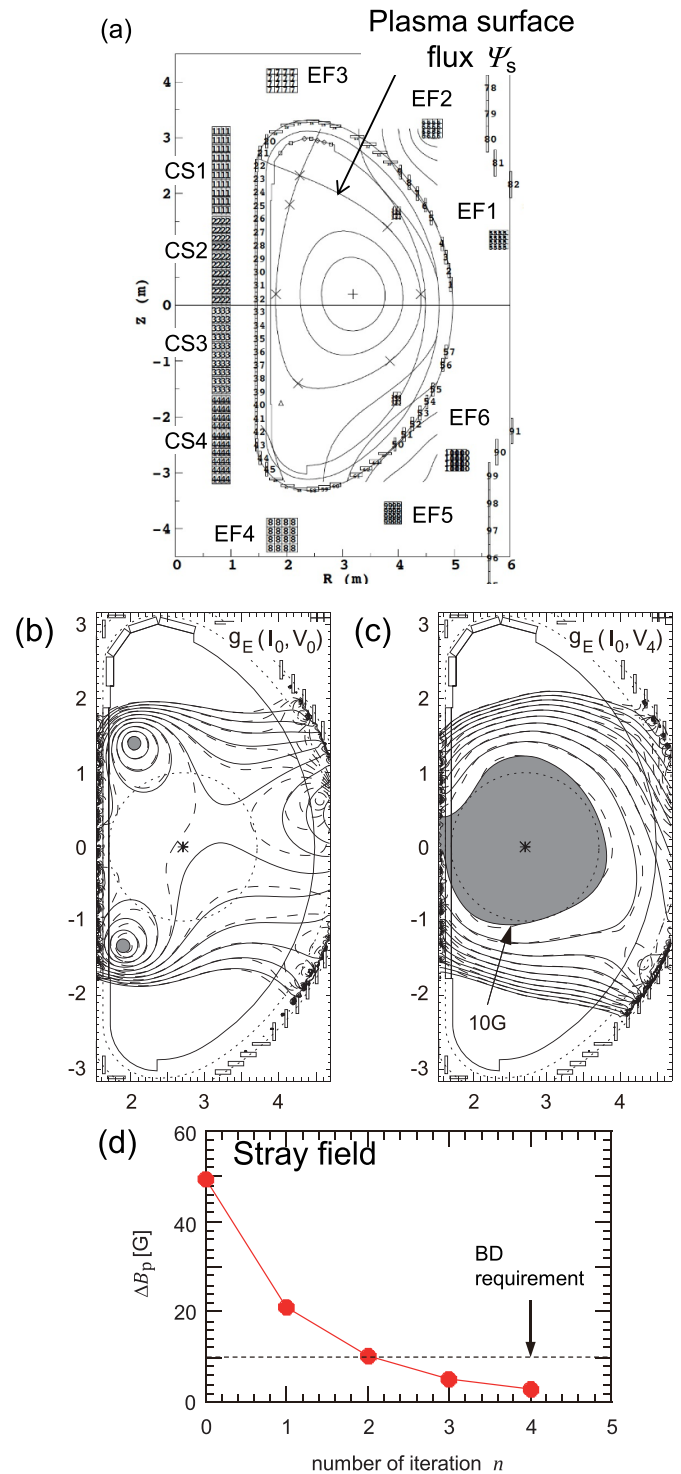

Figure 3. (a) Poloidal coil location and a typical plasma configuration in the early of the Initial Research Phase I. The contours of the stray fields (b) before the iteration of the inverse reconstruction method, and (c) after the 4th iteration. (d) The mean deviation of the stray field strength, ΔB_P in the breakdown target region as a function of the number of iterations, n.

field can be optimized within a couple of shots. As the inverse reconstruction method does not significantly depend on the conducting structure, the inverse reconstruction method could be applied to ITER.
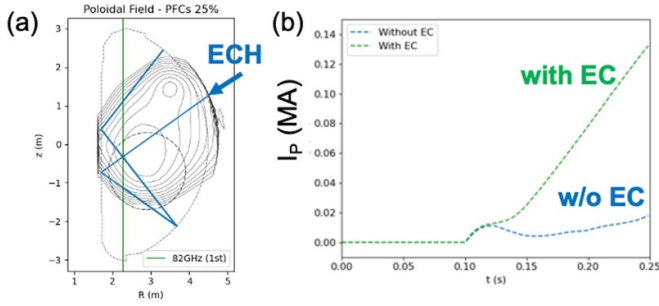
Figure 4. (a) Cross section and the ECH trace simulated by the BKD0 and GRAY codes. (b) Comparison of the plasma current build-up with and without ECH.

Figure 5. (a) Comparison of the maximum plasma current in the discharge started with the TPC and FNC as a function of the D2 prefill pressure in the TST-2 tokamak. Reproduced with modification from figure 7(a) in [13]. (b) Example of TPC in JT-60SA. The EC resonance is shown in red.

The ECH system will assist the plasma breakdown. The effect of ECH on an FNC breakdown is estimated by the suite of codes, BKD0, GRAY, and CREATE-BD [12]. EC waves at the fundamental cyclotron frequency are injected from an oblique upper port, and the power is absorbed through some reflections as shown in figure 4(a). Here the ECH power, gyrotron frequency, prefill gas pressure and the magnetic field are $P_{\mathrm{EC}} = 0.5$ MW, 82 GHz, 1.5 mPa, and $B_{\mathrm{T}} = 2.25$ T, respectively, in the simulations. The plasma current at the build-up phase increases with ECH compared to that without ECH as shown in figure 4(b). The ECH-assisted start-up will expand the breakdown regime to higher pressure, which is a strong requirement at the first operation in any devices.

At the low prefill pressure side, the trapped particle configuration (TPC) can be favorable as demonstrated in the TST-2 tokamak [13]. Figure 5(a) shows the maximum plasma current in the discharge started with the TPC and FNC in TST-2. EC wave was injected with X-mode polarization from the outboard side of the vacuum vessel at a frequency of 2.45 GHz and source power of 5 kW. The maximum plasma current in the discharge started in TPC tends to be higher in the low prefill pressure compared to that in FNC. The low prefill pressure would be beneficial to minimize the magnetic flux consumption, which could result in pulse length extension. In JT-60SA, a TPC with good up-down symmetry can be made even with the horizontal asymmetry of the EF coil positions as shown in figure 5(b). The EC resonance layer at $R \sim 2.27$ m is selected to satisfy the required decay index for the rapid current ramp-up [14]. Both the ohmic plasma and ECH-assisted start-up methods assessed in JT-60SA can contribute to the optimization of start-up scenarios in ITER.

The start-up produced runaway electrons (REs) could be a problem sometime at the first operation of new devices [15]. According to an RE orbit analysis in the FNC with the stray fields, the REs up to 10 MeV are confined at a plasma current above 20 kA. In order to avoid such a runaway beam, the start-up RE free area is estimated by the power balance modeling in the INDEX-S code for JT-60SA start-up plasmas [16]. An example of the plasma current ramp-up free of the RE current with hydrogen prefill gas of 1 mPa is shown in figure 6(a). After the plasma burn-through ($t = 0.3$ s), the volume averaged electron density and temperature, the loop voltage, and the plasma volume during the plasma current ramp-up phase
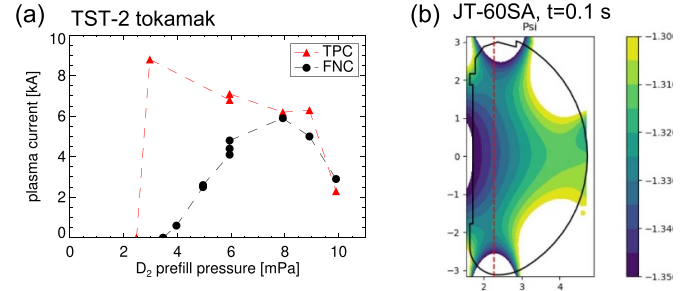
are $n_{\mathrm{e}} = 2.5 \times 10^{18}$ m^{-3}, $<T_{\mathrm{e}} \geqslant 0.12$ keV, $V_{\mathrm{loop}} = 2.1$ V, and 45 m^3, respectively. Figure 6(b) shows a parametric study of generated RE current as a function of the prefill pressure and the electron density and prefill pressure 1 s after the plasma breakdown. Here the hydrogen recycling rate during the breakdown is also varied in a wide range (0.7–1.3) to simulate wall pumping and fueling. It is found that the density build-up to $n_{\mathrm{e}} \sim 10^{18}$–$10^{19}$ m^{-3} will ensure the avoidance of the early RE formation. ECH will be useful to avoid a failure of burn-through at high prefill pressure with impurity radiation. Low-density discharges with low prefill pressure (high E_ϕ/p) also need to be paid attention for the comping operation.

3.2. Equilibrium control

After successful plasma-start up, the next issue is the equilibrium control during the plasma current ramp-up phase in the presence of a large eddy current. The plasma equilibrium will be controlled by the isoflux scheme in JT-60SA [17]. In the isoflux scheme, a proportional-integral derivative (PID) control is adopted for the plasma position or shape and plasma current controls simultaneously. The equation consists of the shape control part and the I_{P} control part having six gains as follows

$$\delta\psi_{\mathrm{S,PID}} = G_{\mathrm{SP}}\delta\psi_{\mathrm{S}} + G_{\mathrm{SI}}\int \delta\psi_{\mathrm{S}}\mathrm{d}t + G_{\mathrm{SD}}\frac{\mathrm{d}\psi_{\mathrm{S}}}{\partial t}$$
$$\delta\psi_{\mathrm{X,PID}} = G_{\mathrm{XP}}\delta\psi_{\mathrm{X}} + G_{\mathrm{XI}}\int \delta\psi_{\mathrm{X}}\mathrm{d}t + G_{\mathrm{XD}}\frac{\mathrm{d}\psi_{\mathrm{X}}}{\partial t}. \quad (1)$$

Here $\delta\psi_{\mathrm{S}}$ and $\delta\psi_{\mathrm{X}}$ are the residual flux values for position/shape and I_{P} controls, and G_{SP}, G_{SI}, G_{SD}, G_{XP}, G_{XI}, and G_{XD} are PID control gains for the position/shape and I_{P} controls. The suffix 'x' stems from the link of the plasma current control to the poloidal magnetic flux at a last closed flux surface (ψ_{X}) as $\delta\psi_{\mathrm{X}} = -L_{\mathrm{i}}\delta I_{\mathrm{p}}$. Here L_{i} is the internal inductance [18]. The key point is to balance between the plasma shape and plasma current controls within the available coil current and voltage. An adaptive voltage allocation (AVA) scheme, which adjusts the control gains automatically to avoid voltage saturation, has been developed [18]. The coil voltage is given as $\boldsymbol{V} = \boldsymbol{F}(\mathrm{G}_{\mathrm{S,AVA}}\boldsymbol{M}^+\delta\psi_{\mathrm{S,PID}} + \mathrm{G}_{\mathrm{X,AVA}}\boldsymbol{M}^+\delta\psi_{\mathrm{X,PID}})$, where $\boldsymbol{F}$ is
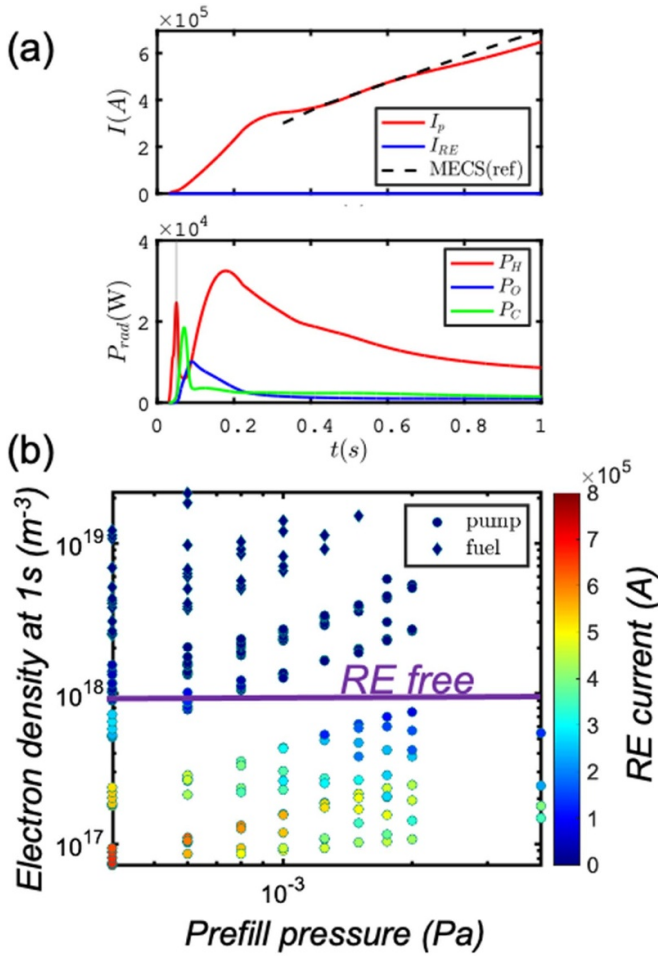
Figure 6. (a) Time evolution of the plasma current, runaway electron, and radiation power from the main gas (hydrogen) and impurities (oxygen and carbon) simulated by the INDEX-S code for a JT-60SA start-up scenario. (b) Start-up runaway electron free area estimated by power balance modeling as functions of the electron density and prefill pressure.

Figure 7. Temporal evolution of (a) the plasma current, (b) the vertical position of the magnetic axis, (c) the automatically adjusted gain, $G_{x,AVA}$. The green and red curves show the cases with and without the adaptive voltage allocation (AVA) scheme, respectively. The blue dashed line shows the reference (or command value) of the plasma current.

a function to transform the residual flux values to the power supply voltages by using circuit equations. The gain, $G_{S,AVA}$ is fixed as unity, and $G_{X,AVA}$ is automatically adjusted according to the weight of the I_P control to the position/shape control. Figure 7 shows simulations to assess the plasma controllability with and without the AVA scheme during the plasma current ramp-up phase on JT-60SA. The position/shape control has higher priority than the I_P control in this simulation in order to avoid the vertical displacement event (VDE). The $G_{X,AVA}$ is automatically reduced from 1 to 0.3 in order to reduce the influence from the I_P control to the position/shape control. Although the control error of the plasma current with the AVA scheme slightly increases compared with that without the scheme, the plasma position control is clearly improved.

The equilibrium control will be investigated for long pulse operation in JT-60SA to confirm equilibrium controllability until flux consumption. The equilibrium reconstruction will be identified by means of some measurements, such as Langmuir probes, soft x-ray array and so on. JT-60SA will provide
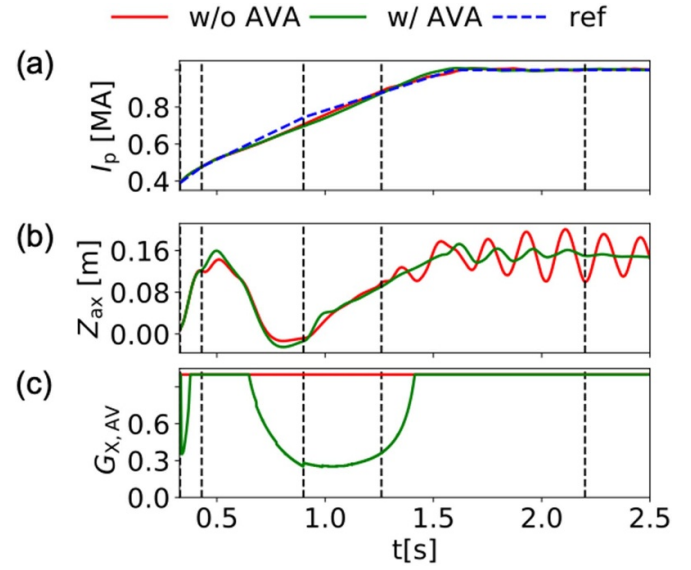
accuracy of equilibrium reconstruction and control at long pulse and flux consumption for ITER inductive operation.

3.3. For ITER and DEMO scenario development

Accessibility of the ITER and DEMO relevant plasma regimes is explored by means of an integrated model GOTRESS+ [19] which consists of the iterative transport solver as a kernel of the integrated model, the equilibrium and current profile alignment code (ACCOME) and the neutral beam heating/current-drive code (OFMC) as shown in figure 8. Both the safety factor and ion temperature profiles are nearly converged after four iterations. This integrated code predicts that an ITER-like plasma regime of $H_{98,y} = 1.0$, $\beta_N = 2.1$, $\kappa_x = 1.81$, $\delta_x = 0.41$, $f_{GW} = 0.79$ can be achieved with 20 MW of heating power ($P_{N-NB} = 10$ MW, $P_{P-NB} = 10$ MW) at $I_p = 4.6$ MA and $B_T = 2.3$ T (the second scenario (II) in table 2). The MHD stability of the converged profile is examined over the entire profile by the MARG2D or MINERVA-DI code [20] as post-processing. The DEMO-relevant steady-state regime of $\beta_N = 4.3$, $H_{98,y} = 1.6$ and $f_{BS} = 0.68$ is achievable with 23 MW ($P_{NBI} = 16.0$ MW and $P_{ECH} = 7.0$ MW) at $I_p = 2.3$ MA and $B_T = 1.7$ T. These results motivate the scenario development for ITER and DEMO in the Initial Research Phase II and the Integrated Research Phase I, respectively.

To access a hybrid plasma, the plasma current profile control during plasma current ramp-up is essential. In JT-60SA the ECH power deposition location is controlled by changing the steerable mirrors for fine-tuning of the plasma current profile. In order to obtain the hybrid scenario in JT-60SA, favorable ECH resonance and ECH power during the current ramp-up
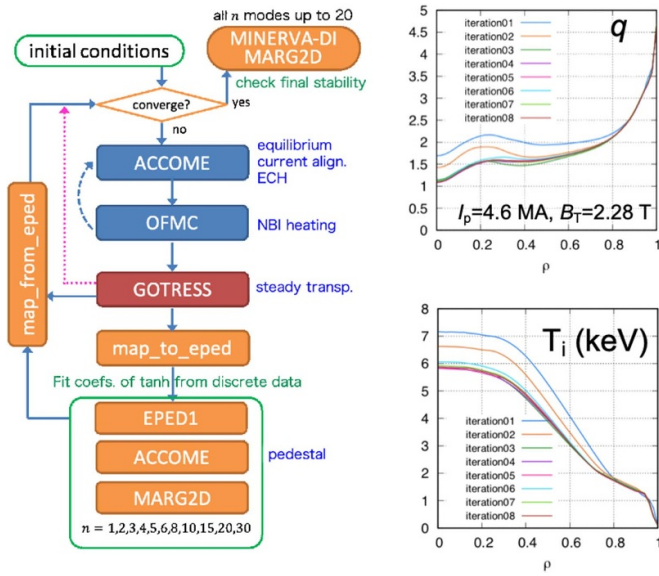
Figure 8. Flowchart of a GOTRESS+ simulation. Converging process of the safety factor, q, and ion temperature, T_i, profiles in the GOTRESS+ simulation for an ITER-like scenario in JT-60SA. The digits in the subfigures denote the iteration number for visibility.

Figure 9. Time evolutions of the plasma current and ECH power simulated by the CRONOS code. (b) ECH power deposition locations and the responses of (c) the safety factor and (d) the electron temperature at $t = 12.5$ s.

phase are explored by using the integrated modeling code CRONOS [21]. Figure 9 shows the current ramp-up scenario simulation in an L-mode phase. Here the target plasma is set to $H_{98,y} = 1.2$, $\beta_N = 3.0$, and $q_{95} = 4.4$ in $I_p = 3.5$ MA and $B_T = 2.3$ T (the third scenario (III) in table 2). The ECH power with 138 GHz (second harmonic resonance) is injected from the plasma breakdown, and the ECH power increases until the L-H transition. The electron temperature becomes higher as the ECH power deposition gets closer to the plasma center, helping delay the plasma current penetration. On the other hand, the on-axis ECH of $\rho \sim 0.23$ pulls the center-q down to less than unity. Here ρ is the normalized plasma radius. The ECH absorption around $\rho \sim 0.33$ allows a compromise between the requirement of $q > 1$ and high central electron temperature. The impact of the plasma current ramp-up rate is also simulated. The ECH power required to obtain $q > 1$ is greater by almost a factor of two when the current ramp up rate is twice faster.

3.4. Physics studies on ITER and DEMO relevant regimes

To access steady-state plasma regimes, off-axis N-NBs will be injected during current ramp-up phases in JT-60SA. This operation tends to induce MHD and resonant instabilities with a steep gradient of the beam driven plasma current and fast ion pressure. An exhaustive kinetic-hybrid MHD analysis using the MEGA code had been performed [22]. In order to compare and extend this analysis with gyrokinetic (GK) linear simulations, an interface between the MEGA-generated EP distribution functions and LIGKA has been developed [23]. Toroidal Alfvén eigenmodes (TAE) can be unstable over the whole radius due to a weak damping of the TAE modes during the current ramp-up phase. The JT-60SA current ramp-up will be a good testbed to validate and improve the code. Then the
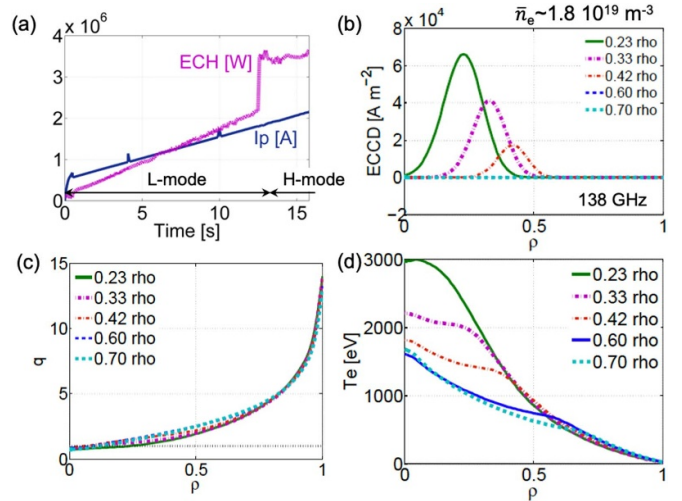
code will provide validated evaluation of the heating and current drive efficiency in the future machines, ITER and DEMO.

As mentioned in section 2 and figure 2, it will be one of the important contributions to validate turbulence transport models by means of experiments in the ITER and DEMO-relevant regimes. A preparatory study of the plasma shape sensitivity to microturbulence instabilities has been investigated [24]. Here the GK simulation code GS2 is used [25]. Figure 10 shows the contour plot of the turbulence growth rates on the elongation and triangularity calculated by the GK stability analyses. The nominal shape is indicated by the black cross. The kinetic ballooning modes (KBMs) can be dominant due to the high beta value and large pressure gradient. Here the modes are identified by a step change in the real frequency of the analyses. If the elongation and/or triangularity increase, KBMs can be stabilized. Another analysis on non-linear electrostatic scans give an increase of the zonal flow energy with increasing elongation. The trend reflects the reduction in the turbulent transport with elongation. These theoretical analyses will be repeated with measured density and temperature profiles. In order to increase the understanding of the physics behind and to strengthen the model validation, feasibility and design studies on the measurements of the fast ion losses [26] and fluctuation covering the low-k to higher-k regimes [27–29] are ongoing.

4. ITER risk mitigation

JT-60SA will play an important role in reducing the risks in ITER operation, taking advantage of its characteristics, including high plasma current, high heat and particle flux and low collisionality. Control studies of the three major risks, namely disruption, large ELMs and steady heat load to the divertor, will be efficiently performed by exploiting the machine conditions in each research phase. As most of the research items
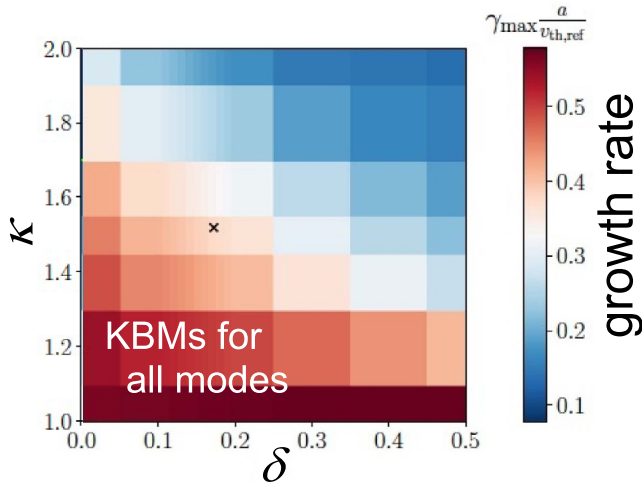
Figure 10. Counter plot of the maximum linear growth rates in the elongation, κ and triangularity, δ analyzed by the CS2 code. The fastest growing mode are KBMs for the simulated regimes of κ and δ. The nominal value of a high β operation is shown by cross.

Figure 11. Temporal evolution of (a) I_P, (b) vertical position, Z_{ax} and (c) velocity of current centroid, v, and (d) automatically controlled gain for position and shape, $G_{s,AVA}$ simulated by the MECS code. Red dashed lines indicate a natural VDE, blue solid lines indicate a controlled VDE. VDE predicted region (filled), which are projected to (e) (decay index, n and v) and (f) (n, GS,AVA) plane. Typical simulation data from I_P ramp-up to flat-top without VDE are also shown by dot points.

also relate to issues in DEMO, the risks of DEMO can be also reduced through the ITER risk mitigation studies. This section describes simulation studies on a VDE control, large ELM control by pellet injection, and heat load handling by impurity seeding.

4.1. VDE control

VDEs often cause or accompany disruptions. A control scheme of VDEs has been developed with machine learning and the AVA scheme [18]. Figure 11 shows the time histories of the plasma current, vertical position, vertical velocity and $G_{s,AVA}$ in MECS simulations. Here $G_{s,AVA}$ (defined in section 3.2) is introduced to avoid a coil voltage saturation. In other words, $G_{s,AVA}$ represents voltage saturation rates ($\leqslant 1$) necessary to compensate the residual flux for position/shape control. When a minor collapse with 1% of plasma current happens, the amplitude of the vertical velocity increases and $G_{s,AVA}$ decreases. Then a downward VDE occurs as shown by the dashed red lines in figure 11(b). The VDE direction is controlled as indicated by the blue solid lines using the VDE control technique. By focusing on pre-VDE behaviors, namely the increase in the vertical velocity and the decrease in $G_{s,AVA}$, a machine learning algorithm is applied to the VDE prediction using the vertical velocity, $G_{s,AVA}$, and the decay-index, n as shown in figures 11(e) and (f). The VDE unstable region shown in red is decoupled of the VDE stable traces shown in black dots. The VDE predictor can be applied to ITER, for instance, to give a favorable time of the shattered pellet injection in order to mitigate the VDE driven disruptions. Also, the vertical stability controller can be used for deliberate upward and downward VDEs in the electromagnetic load testing [30].

Asymmetric and rotating VDEs might lead to large uncertainties in the forces applied to the ITER vacuum vessel and blanket. JT-60SA is well-suited to perform such VDE
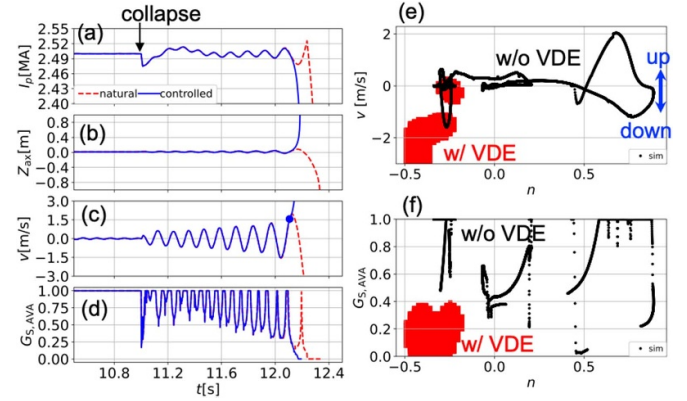
asymmetry studies. The halo current can be measured by Rogowski coils installed under the CFC targets at some of the 36 divertor cassettes, distributed at the bottom of the vacuum vessel. The long wall constant ($\tau_{wall} \approx 65$ ms), high energy content (20 MJ), high plasma current (5.5 MA) and energetic ions with 500 kV N-NB are beneficial to validate models and simulation codes for the VDE and disruption studies.

4.2. ELM mitigation

The ELM control at low ν^* will be developed to find regimes which are compatible with favorable confinement and internal transport barriers. The ELM controllability has been assessed with linear and non-linear MHD codes when using magnetic perturbations [31] and pellets [32]. Recently, the pellet triggered ELM behavior has been simulated by the nonlinear code, JOREK [33–35] to find an optimized operational window for the ELM mitigation in JT-60SA at $I_P = 5.5$ MA, $B_T = 2.25$ T, $P_{in} = 41$ MW and single null divertor (the first scenario (I) in table 2). When the pellets are injected from the high field side with an injection angle of 80° [36], a very localized expansion of ballooning mode structures appears together with the expansion of the pellet clouds. Figures 12(a) and (b) show the density and potential contour plots for the pellet triggered ELM and a spontaneous ELM, respectively, at the time of maximum pellet ablation for the pellet size of 1.5×10^{20} D. The ballooning mode structures in the pedestal region during the pellet triggered ELM show larger structures in the X-point region compared to the spontaneous ELM. This is due to the pellet cloud which is propagated along the magnetic field line from the pellet injection location. The pellet cloud creates the density and the pressure perturbation, which contributes to the ballooning mode structures [37].

The pellet injection time and pellet size are scanned at a constant injection velocity of 400 m s^{-1} to carry out efficient

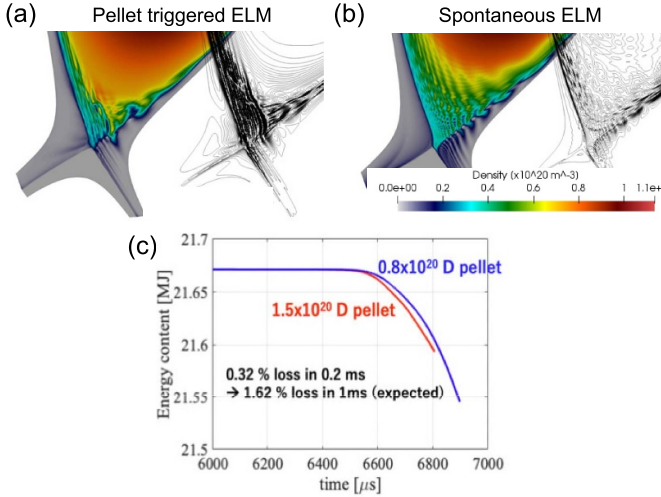(a) Pellet triggered ELM (b) Spontaneous ELM

(c)

Figure 12. Contour plots of density (colored) and potential (lined) at (a) a pellet triggered ELM and (b) a spontaneous ELM at the maximum pellet ablation rate with the pellet size of 1.5×10^{20} D simulated by the JOREK code. (c) Time evolution of energy content inside the separatrix during the pellet-triggered ELM with the pellet sizes of 1.5×10^{20} D (red) and 0.8×10^{20} D (blue).

Figure 13. (a) Profiles of the ion temperature, T_i, the electron temperature, T_e, the safety factor, q simulated by the TOPICS code. The electron density, n_e is prescribed. (b) Computational grid of SONIC in view of the divertor region of JT-60SA. Ar and Ne injection is also indicated. Stacked radiation power of each impurity species (c) in the inner divertor region, $P_{\mathrm{rad,ID}}$ and (d) in the core edge $P_{\mathrm{rad,edge}}$.

ELM mitigation experiments in JT-60SA. The pellet injection time is more important than the pellet size. Both sizes of the pellets of 0.8×10^{20} D and 1.5×10^{20} D trigger the ELMs when those are injected just before the pre-ELM phase. This is because the plasma is already approaching a spontaneous ELM crash at the pre-ELM phase. The pellets reach the full ablation at the radial position of $\psi N = 0.96$ and $\psi N = 0.95$ with the size of 0.8×10^{20} D and 1.5×10^{20} D pellets, respectively. Here the pedestal top of is $\psi N = 0.93$. Figure 12(c) shows the time evolution of the energy content after the pellet injection for the two pellet sizes. The ELM energy loss is about 1.6% of the total stored energy, that is smaller than the natural ELM by about a factor of 5. On the other hand, no trigger is predicted, even if the larger pellet of 1.5×10^{20} D is injected in the post-ELM phase.

4.3. Heat load handling

The divertor heat load handling schemes by impurity seeding are investigated in several cases. The low-density detached regime will be explored by impurity compression. Simulation codes will be validated by means of detached divertor observations in order to understand the physics and improve the predictive basis for ITER and DEMO.

A full-scale steady-state high β plasma with radiative divertor will be assessed in the metallic wall phase, i.e. in the Integrated Research Phase II. On the other hand, the physics mechanism of the compatibility between high β_N plasma and radiative divertor can be studied in the carbon wall phase, i.e. from the Initial Research Phase II. A simulation study of multi-impurity seeding has been done with the integrated divertor code SONIC [38]. Development of the steady-state scenario is planned at medium plasma current of ≈ 2.3 MA,
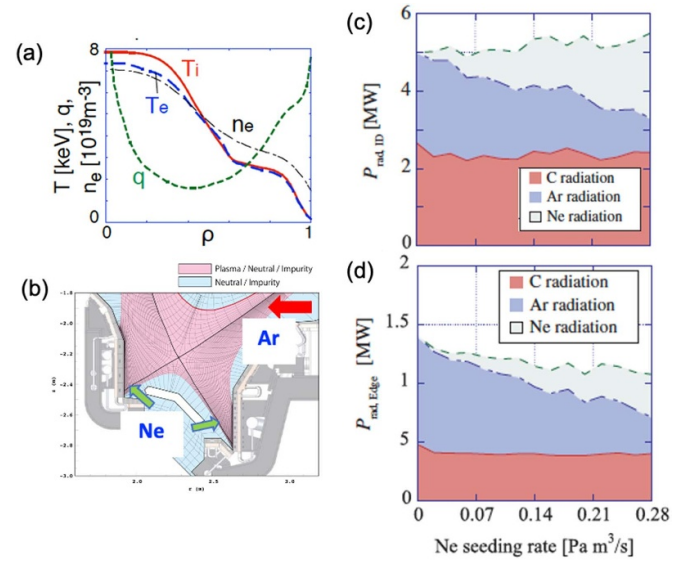
$B_T \approx 1.72$ T and $q_{95} \approx 5.8$ with a DEMO-like shape configuration of $A \approx 2.7$, $\delta_x \approx 0.47$, $\kappa_x \approx 1.91$, and $S \approx 7.0$ (the forth scenario in table 2). The simulation indicates that a higher radiation power in the divertor region and a lower radiation power in the core-edge region can be realized with the mixed-impurity seeding of Ar and Ne, rather than the Ar only case. Figure 13 show the radiation power from the C, Ar and Ne impurity species as a function of the Ne seeding rate in the inner divertor and those in the plasma edge region. Here a parametric survey of Ne seeding at a constant Ar puff rate of 0.2 Pa m^3 s^{-1} is performed. The radiation power of Ar impurity decreases with increasing Ne seeding rate in the core-edge region. The mechanism stems from the change in the force balance. In the Ar only seeding case, Ar impurities stagnate at the top of the scrape-off layer (SOL) region. In the Ar and Ne seeding case, the Ar impurities are transported to the inner divertor region.

Edge and divertor modeling in the highest plasma current case of $I_P = 5.5$ MA, $B_T = 2.25$ T, highest heating power of $P_{in} = 41$ MW, and low separatrix density of $n_{e,sep} = 2.0 \times 10^{19}$ m^{-3} (the first scenario in table 2) with carbon wall have been performed with the SOLEDGE2D-EIRENE code [39]. Figure 14 illustrates the divertor heat load as a function of Ar seeding rate. Here the total heat flux to the SOL region is given as a constant value of 30 MW, and the carbon impurity radiation power is about 8 MW. The power heat load onto the outer target decreases with increasing Ar influx and reaches a target value of 10 MW m^{-2}. The plasma purity defined as the deuterium ion density divided by the electron density, $n_{D,sep}/n_{e,sep}$ at the separatrix remains around 70%–80%; here the Z_{eff} is around 2.8–3.1.
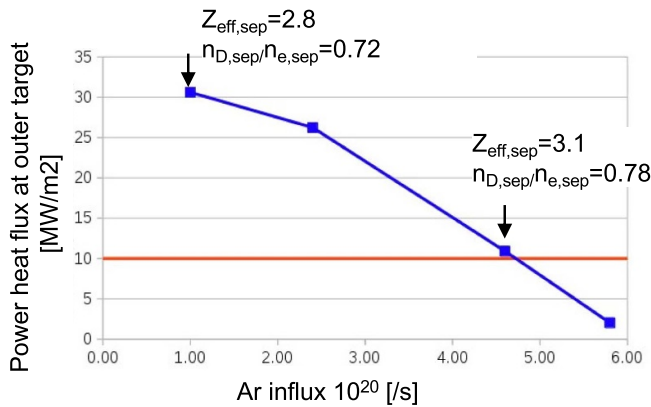
Figure 14. Ar seeding rate dependence of the power heat flux at the outer target. The heat flux decreases from 30 MW m^{-2} to the target value of 10 MW m^{-2} with Ar seeding with a small increment of Z_{eff} at the separatrix.
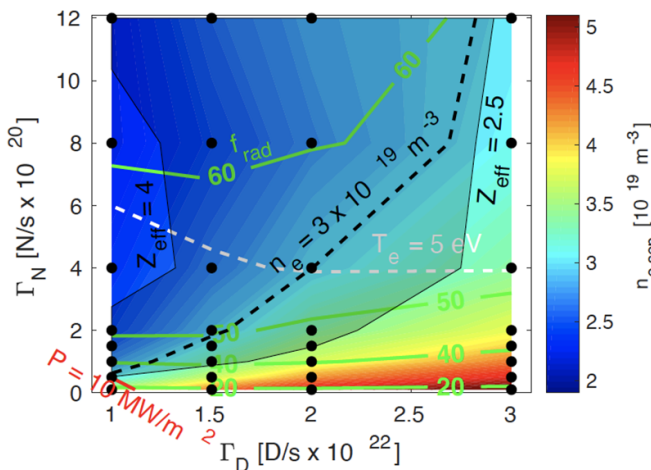

Figure 15. Operational window of the technological limits for the deuterium flux, Γ_D and nitrogen flux, Γ_N scans. Contour levels at the separatrix density, $n_{e,sep} = 3 \times 10^{19}$ m^{-3}, the maximum heat flux at divertors, $P = 10$ MW m^{-2} and the electron temperature at the $T_e = 5$ eV are respectively shown in black, red and white. Green lines represent contour lines for f_{rad}.

Compatibility of long-pulse high-β_N and radiative plasmas with metal plasma-facing components will be explored in the Integrated Research Phase II. Assessment of divertor plasma conditions with a tungsten wall in a high-density scenario of $nl = 1.0 \times 10^{20}$ m^{-3} ($f_{GW} = 0.8$ at $I_P = 5.5$ MA) with the injection power of 30 MW is made with the SOLPS-ITER code suite [40]. Here nl is the line averaged density. Nitrogen seeding is adopted, based on the cooling performance in metallic devices [41, 42]. The operation conditions to reach a criteria of heat flux to the divertor of 10 MW m^{-2} and a detachment divertor condition of $T_e < 5$ eV are imposed for the auxiliary power of 30 MW and the power flux through the separatrix of 20 MW. The operational window in terms of the nitrogen and deuterium gas puffing rates is shown in figure 15. The operational window is delimited by the T_e limit of 5 eV. The target of power heat flux of 10 MW m^{-2} is fulfilled for most of the region shown in figure 15. Relatively wide operation windows

for the separatrix density of $n_{e,sep} \sim 3.0 \times 10^{19}$ m^{-3}, the plasma radiation function of $f_{rad} \sim 0.5$–0.6, and $Z_{eff,sep} \sim 2.5$–4.0 are obtained. The momentum loss caused by the collisions between deuterium ions and deuterium molecules is the main driver for detachment onset when the electron temperature becomes low enough to trigger the detachment.

5. Summary

JT-60SA will contribute to the early realization of fusion energy by addressing key physics issues for ITER and DEMO. Preparatory simulation studies about the plasma control for the scenario development and risk mitigation on JT-60SA are highlighted in this paper. The plasma breakdown optimization has been investigated by the inverse reconstruction method, ECH assist, and assessment of the start-up runaway free area. The AVA logic is developed for the robust equilibrium control. The favorable ECH deposition control during the I_P ramp-up phase is simulated to obtain a hybrid operation. To increase the core confinement, microturbulence and fast ion driven modes sensitivities to the plasma shape and kinetic profiles are assessed using linear and non-linear GK or gyrofluid codes. Some risk mitigation methodologies have been designed: VDE prediction and control using machine learning algorithms and an AVA scheme, large ELM mitigation by pellets, and divertor heat load handling by multi-impurity seeding. For these simulations, the appropriate integrated simulation codes have been developed. The major issues of the plasma physics and control studies will be performed in ITER and DEMO relevant regimes by the JT-60SA Experiment Team in order to contribute to both ITER operation and DEMO design.

Data availability statement

The data that support the findings of this study are available upon reasonable request from the authors.

ORCID iDs

M Yoshida ⓘ https://orcid.org/0000-0002-2899-1323
G Giruzzi ⓘ https://orcid.org/0000-0001-9628-5968
J Ayllon-Guerola ⓘ https://orcid.org/0000-0001-8127-3921
J Garcia ⓘ https://orcid.org/0000-0003-0900-5564
C Sozzi ⓘ https://orcid.org/0000-0001-8951-0071
H Urano ⓘ https://orcid.org/0000-0001-8740-8954

References

[1] JT-60SA Research Unit, 'JT-60SA Research Plan 2018 Research objectives and strategy', v4.0 September (available at: http://jt60sa.org/pdfs/JT-60SA_Res_Plan.pdf)
[2] Tobita K *et al* 2019 *Fusion Sci. Technol.* **75** 372–83
[3] Kamada Y *et al* 2022 *Nucl. Fusion* **62** 042002
[4] Wan B N *et al* 2017 *Nucl. Fusion* **57** 102019
[5] Kwak J-G *et al* 2013 *Nucl. Fusion* **53** 104005
[6] Bucalossi J *et al* 2014 *Fusion Eng. Des.* **89** 907
[7] Joffrin E *et al* 2019 *Nucl. Fusion* **59** 112021
[8] Petty C C *et al* 2019 *Nucl. Fusion* **59** 112002
[9] Coda S *et al* 2019 *Nucl. Fusion* **59** 112023
[10] Giruzz G *et al* 2020 *Plasma Phys. Control. Fusion* **62** 014009
[11] Urano H, Miyata Y, Suzuki T and Kurihara K 2020 *Nucl. Fusion* **60** 66002
[12] Ricci D *et al* 2019 *46th EPS Plasma Physics Conf.* (*Milano*) O5.103
[13] Ko Y *et al* 2021 *Plasma Fusion Res.* **16** 1402056
[14] Uchida M, Maekawa T, Tanaka H, Ide S, Takase Y, Watanabe F and Nishi S 2011 *Nucl. Fusion* **51** 063031
[15] Reux C *et al* 2021 *2020 28th IAEA Fusion Energy Conf.* (Virtual Event) EX/P5-5
[16] Matsuyama A and Yagi M 2017 *Plasma Fusion Res.* **12** 1403032
[17] Miyata Y, Hahn S H, Suzuki T, Ide S, Chung J, Bak J G and Ko W H 2014 *Phys. Plasmas* **21** 032502
[18] Inoue S, Miyata Y, Urano H and Suzuki T 2021 *Nucl. Fusion* **61** 096009
[19] Honda M, Aiba N, Seto H, Narita E and Hayashi N 2021 *Nucl. Fusion* **61** 116029
[20] Aiba N *et al* 2016 *Plasma Phys. Control. Fusion* **58** 045020
[21] Morales J, Garcia J, Giruzzi G, Artaud J-F, Piron C, Vallar M and Goodman T 2021 *Plasma Phys. Control. Fusion* **63** 025014
[22] Bierwage A, Toma M and Shinohara K 2017 *Plasma Phys. Control. Fusion* **59** 125008
[23] Lauber P *et al* 2021 *2020 28th IAEA Fusion Energy Conf.* (Virtual Event) TH/P1-20
[24] Beeke O, Barnes M, Romanelli M, Nakata M and Yoshida M 2021 *Nucl. Fusion* **61** 066020
[25] Kotschenreuther M, Rewoldt G and Tang W M 1995 *Comput. Phys. Commun.* **88** 128
[26] Ayllon-Guerola J *et al* 2021 *Fusion Eng. Des.* **167** 112304
[27] Coda S *et al* 2021 *2020 28th IAEA Fusion Energy Conf.* (Virtual Event) TH/P7-31
[28] Tokuzawa T *et al* 2019 *2019 14th Int. Reflectometry Workshop* (*Lausanne, Switzerland*) O.203 (https://doi.org/10.1103/PhysRevLett.123.185001)
[29] Carralero D, Happel T, Estrada T, Tokuzawa T, Martínez J, de la Luna E, Cappa A and García J 2021 *Fusion Eng. Des.* **173** 112803
[30] ITER Organization 2018 ITER research plan within the staged approach (level III—provisional version)
[31] Pamela S *et al* 2018 *2018 27th IAEA Fusion Energy Conf.* (*Ahmedabad, India*) OV/4-4
[32] Futatani S, Huijsmans G, Loarte A, Baylor L R, Commaux N, Jernigan T C, Fenstermacher M E, Lasnier C, Osborne T H and Pegourié B 2014 *Nucl. Fusion* **54** 073008
[33] Huysmans G and Czarny O 2007 *Nucl. Fusion* **47** 659
[34] Czarny O and Huysmans G 2008 *J. Comput. Phys.* **227** 7423
[35] Hoelzl M *et al* 2021 *Nucl. Fusion* **61** 06500
[36] Lang P T, Nakano T, Davis S, Matsunaga G, Pégourié B, Ploeckl B and Treuterer W 2019 *Fusion Eng. Des.* **146** 91–95
[37] Futatani S *et al* 2021 *2020 28th IAEA Fusion Energy Conf.* (Virtual Event) TH/P6-21
[38] Yamoto S, Hoshino K, Homma Y, Nakano T and Hayashi N 2020 *Plasma Phys. Control. Fusion* **62** 045006
[39] Balbinot L *et al* 2019 *2019 3rd IAEA Technical Meeting on Divertor Concepts* (Virtual Event) p 53
[40] Rubino G, Calabrò G and Wischmeier M 2021 *Nucl. Mater. Energy* **26** 100895
[41] Giroud C *et al* 2015 *Plasma Phys. Control. Fusion* **57** 035004
[42] Kallenbach A *et al* 2010 *Plasma Phys. Control. Fusion* **52** 055002